DIRECT-FOURIER RECONSTRUCTION IN TOMOGRAPHY AND SYNTHETIC APERTURE RADAR *

Hyeokho Choi and David C. Munson, Jr. †

Abstract

We investigate the use of direct-Fourier (DF) image reconstruction in computerized tomography and synthetic aperture radar (SAR). One of our aims is to determine why the convolution-backprojection (CBP) method is favored over DF methods in tomography, while DF methods are virtually always used in SAR. We show that the CBP algorithm is equivalent to DF reconstruction using a Jacobian-weighted 2-D periodic sinc-kernel interpolator. This interpolation is not optimal in any sense, which suggests that DF algorithms utilizing optimal interpolators may surpass CBP in image quality. We consider use of two types of DF interpolation: a windowed sinc kernel, and the least-squares optimal Yen interpolator. Simulations show that reconstructions using the Yen interpolator do not possess the expected visual quality, because of regularization needed to preserve numerical stability. Next, we show that with a concentric-squares sampling scheme, DF interpolation can be performed accurately and efficiently, producing imagery that is superior to that obtainable by other algorithms. In the case of SAR, we show that the DF method performs very well with interpolators of low complexity. We also study DF reconstruction in SAR for trapezoidal grids. We conclude that the success of the DF method in SAR imaging is due to the nearly-Cartesian shape of the sampling grid.

*This work was supported by the Joint Services Electronics Program (U. S. Army, Navy, Air Force) under Contract N00014-90-J-1270.

†H. Choi and D. C. Munson, Jr. are with the Coordinated Science Laboratory and Department of Electrical and Computer Engineering, University of Illinois at Urbana-Champaign, Urbana, IL 61801.

List of Tables

1 Squared error of reconstructed images - CBP, and DF with sinc interpolation 25

2 Squared error of reconstructed images - block-Yen algorithm 25

3 Squared error of reconstructed images - block-Yen with $\epsilon = 10^{-4}$ 25

4 Squared error of reconstructed images - CS grid 25

5 Squared error of reconstructed images - SAR 26

List of Figures

1 Fourier grid cell 27

2 Original image. 27

3 CT reconstruction produced by CBP algorithm. 27

4 CT reconstruction produced by equivalent direct-Fourier method. 28

5 CT reconstruction produced by direct-Fourier method using 4×4 sinc interpolator. 28

6 CT reconstruction produced by direct-Fourier method using 16×16 sinc interpolator. 28

7 CT reconstruction produced by direct-Fourier method using 2×2 Yen interpolator, 50 samples maximum, $\epsilon = 10^{-4}$. 28

8 CT reconstruction produced by direct-Fourier method using 2×2 Yen interpolator, 300 samples maximum, $\epsilon = 10^{-4}$. 29

9 CT reconstruction produced by direct-Fourier method using 4×4 Yen interpolator, 50 samples maximum, $\epsilon = 10^{-4}$. 29

10 CT reconstruction produced by direct-Fourier method using 4×4 Yen interpolator, 300 samples maximum, $\epsilon = 10^{-4}$. 29

11 Concentric-squares grid 30

12 Region I grid 30

13 Extra projections in Region I 30

14 CT reconstruction produced by chirp-z algorithm from CS grid with 512 projections. 31

15 Partitioning of Region I 31

16 Location of SAR data on the Fourier plane 31

17 SAR reconstruction from Cartesian Fourier data, $BW/\omega_0 = 0.1024$, $\theta = 5.8672$ degrees. 32

18 SAR reconstruction from polar data, without interpolation, $BW/\omega_0 = 0.1024$, $\theta =$ 5.8672 degrees. 32
19 SAR reconstruction with 4×4 sinc interpolator, $BW/\omega_0 = 0.1024, \theta = 5.8672$ degrees. 32
20 SAR reconstruction with 4×4 Yen interpolator, $BW/\omega_0 = 0.1024, \theta = 5.8672$ degrees. 32
21 Trapezoidal grid in Fourier domain 33

1 Introduction

Computerized tomography (CT) and spotlight-mode synthetic aperture radar (SAR) are examples of imaging systems that can be modeled as acquiring Fourier data that are then inverted to produce an estimate of the cross-sectional density, reflectivity or other quantity of interest. Fourier data can be obtained in CT by computing one-dimensional (1-D) Fourier transforms of the projection data, whereas in SAR, the Fourier data are obtained directly from the radar receiver. In CT, the most popular inversion method is the convolution backprojection (CBP) algorithm, which gives fairly good quality reconstructions, except in the limited-angle scenario. SAR imaging generally employs direct Fourier (DF) reconstruction, whereby the Fourier data are interpolated to a Cartesian grid and then inverted using a fast Fourier transform (FFT).

The possibility of DF reconstruction in tomography has received extensive study [1]-[11]. In [1], the general problem of image reconstruction from projections was discussed. Reconstruction from a polar raster using linear interpolation and the so-called polar expansion algorithm were developed. This paper also proposed another reconstruction method based on a direct approximation of the Fourier inversion formula, using a two-dimensional (2-D) trapezoidal rule. In addition, the possibility of reconstruction from a concentric-squares raster was discussed. Numerous simple interpolators have been tried in DF reconstruction with the results compared with CBP [2]. In [3] and [4], the concept of angular bandlimiting was used to interpolate the polar data onto a Cartesian grid. In [5], a DF reconstruction, using bilinear interpolation for diffraction tomography, provided image quality that was comparable to that produced by the CBP algorithm. Very good reconstruction quality was obtained in [6] and [7] using a spline interpolator, or a hybrid type of spline interpolator. The notion of "gridding" was introduced in [8] as a method of obtaining optimal inversion of Fourier data. An optimal gridding function was proposed, and successful results were obtained when applied to the tomographic reconstruction problem. In [9], several different gridding functions were tried for DF reconstruction, and the performances were compared. In [10, 11], the linogram reconstruction method was proposed as a form of DF reconstruction. The data collection grid in the linogram method is the same as in the concentric-squares sampling scheme. The inversion of the Fourier data in [10, 11] was accomplished by first applying the chirp-z transform in one direction and then computing FFTs in the other direction.

In CT, many of these attempts at DF reconstruction have given a poorer result than the CBP algorithm, due to the error incurred in the process of the polar-to-Cartesian interpolation. The

attraction of DF reconstruction, however, is that it is thought to require less computation than CBP, with the possibility of comparable image quality. The CBP algorithm has been used in commercial CT scanners because it achieves good image quality with a moderate amount of computation.

Spotlight-mode SAR collects Fourier data on a polar grid [12], similar to CT [13]. In SAR, data are usually available only in a narrow angular sector of the polar grid, offset from the origin. Because of the coherent nature of the system [14], these bandpass data contain sufficient information to provide a high-quality image reconstruction. In SAR, the DF method is the image formation technique of choice. We hypothesize that this is because the small sector of the polar grid that arises in SAR is much closer to Cartesian than is the full polar grid in CT. Thus, low-order interpolators can provide good image quality in SAR, whereas they cannot in CT. Furthermore, in SAR, other processing, such as autofocusing [15], is performed on the Cartesian Fourier data. Because this processing begins in the Fourier domain, it is natural to use a DF reconstruction method.

In this paper, we investigate DF image reconstruction in CT and SAR. We begin by showing that the CBP algorithm in CT is equivalent to a DF method with a weighted 2-D periodic sinc-kernel interpolator. This interpolator is not optimal for polar-to-Cartesian interpolation, which suggests that a DF approach with optimal interpolation may actually surpass CBP in terms of image quality. We consider two types of DF interpolation: a windowed sinc kernel, and the least-squares optimal interpolator by Yen [16]. The Yen approach suffers from numerical ill-conditioning. We show that a regularized version of the Yen interpolator is superior to CBP in terms of squared error, but inferior in terms of image quality. When operating on concentric-squares grids, we demonstrate that DF reconstruction can achieve superb CT image quality. In the case of SAR, we show that the DF method performs very well, with polar-to-Cartesian interpolators of low complexity. We also examine DF reconstruction in SAR, for trapezoidal Fourier data grids.

Section 2 proves that the CBP algorithm is equivalent to a DF reconstruction using a 2-D periodic sinc-kernel interpolator. Section 3 introduces the Yen interpolator. In Section 4, we provide simulation results for both the Yen interpolator and a truncated sinc-kernel interpolator in CT image reconstruction. The difficulties involved in using the Yen interpolator are discussed. In Section 5, we investigate the Fourier inversion problem for CT data lying on a concentric-squares grid. Section 6 discusses DF reconstruction in SAR and gives simulation results that are compared with those for CT. Section 7 discusses the SAR reconstruction problem for data lying on a trapezoidal grid. Finally, Section 8 summarizes the results presented in this paper.

2 A Direct-Fourier Interpretation of the Convolution Backprojection Algorithm

The CBP algorithm has been used almost exclusively in practical CT reconstruction, because it provides good image quality at modest computational cost. Although DF reconstruction can be computationally efficient, the DF approach has usually resulted in poorer image quality than CBP. One might suspect that the CBP algorithm is superior to any DF reconstruction algorithm. We will show in this section, however, that the CBP algorithm can be viewed as an efficient implementation of a DF method, using a 2-D periodic sinc kernel in the polar-to-Cartesian interpolation. This leaves open the possibility that DF methods may exist that can outperform CBP in terms of image quality. The relationship between CBP and a DF reconstruction using 2-D Jacobian-weighted sinc-kernel interpolation was discussed briefly in [17]. In our paper, we more thoroughly analyze and compare these reconstruction methods.

In parallel-beam CT[1], projections of an object are collected from many angular directions. If the sampling of the projection data is dense enough so that the effect of aliasing can be ignored, radial slices of the 2-D Fourier transform are obtained by computing a 1-D FFT of each projection. We begin our formulation with Fourier data on a uniform polar grid, rather than with projections in the spatial domain. The polar form of the 2-D inverse Fourier transform is

$$f(x,y) = \int_0^{2\pi} \int_0^{\infty} F_p(\Omega,\theta) \exp[j\Omega(x\cos\theta + y\sin\theta)]\Omega d\Omega d\theta, \tag{1}$$

where $F_p(\Omega,\theta)$ is the 2-D Fourier transform of $f(x,y)$, the absorption profile of the object, in polar coordinates. In our discussion, we assume that $f(x,y)$ is spatially limited to a rectangular region; specifically,

$$f(x,y) = 0 \text{ if } |x| > a \text{ or } |y| > b. \tag{2}$$

The CBP algorithm can be obtained by rewriting Eq. (1) as

$$\begin{aligned} f(x,y) &= \int_0^{\pi} \int_0^{\infty} F_p(\Omega,\theta) \exp[j\Omega(x\cos\theta + y\sin\theta)]\Omega d\Omega d\theta \\ &\quad + \int_0^{\pi} \int_0^{\infty} F_p(\Omega,\theta+\pi) \exp(j\Omega[x\cos(\theta+\pi) + y\sin(\theta+\pi)])\Omega d\Omega d\theta. \end{aligned} \tag{3}$$

Using the property that $F_p(\Omega,\theta+\pi) = F_p(-\Omega,\theta)$, $f(x,y)$ can be written as

$$f(x,y) = \int_0^{\pi} \int_{-\infty}^{\infty} F_p(\Omega,\theta)|\Omega| \exp(j\Omega t) d\Omega d\theta, \tag{4}$$

[1] We consider *parallel-beam* CT because of its mathematical simplicity and its similarity to SAR. Also, modified parallel-beam reconstruction algorithms are sometimes used in fan-beam CT.

where $t = x\cos\theta + y\sin\theta$. The CBP algorithm follows by discretizing the above double integral. (In practice, the Fourier data $F_p(\Omega,\theta)$ are available only at discrete points.) Suppose $F_p(\Omega,\theta)$ are available at $\Omega = p\Delta\Omega$, $p = -\infty,\cdots,\infty$ and $\theta = q\Delta\theta$, $q = 0,1,\cdots,Q-1$, where $\Delta\theta = \pi/Q$. Then, $f(x,y)$ can be approximated as

$$f(x,y) \simeq \sum_{q=0}^{Q-1}\sum_{p=-\infty}^{\infty} F_p(p\Delta\Omega, q\Delta\theta)|p\Delta\Omega|\exp(j\Delta\Omega\cdot p\cdot t)\Delta\Omega\Delta\theta, \tag{5}$$

where $t = x\cos(q\Delta\theta) + y\sin(q\Delta\theta)$. In an actual implementation of the CBP algorithm, the inner summation is approximated by a 1-D FFT, and the outer summation corresponds to the backprojection step of the algorithm. Let $f[n,m] = f(n\Delta_x, m\Delta_y)$ be the discretized samples of $f(x,y)$ where $n = -N,\cdots,0,\cdots,N$ and $m = -N,\cdots,0,\cdots,N$. Approximating the inner summation in Eq. (5) by a 1-D FFT corresponds to truncating the sum at $p = \pm P$, where P is chosen large enough to incorporate all Fourier data samples having significant magnitude[2]. Doing so gives

$$\begin{aligned} f[n,m] \simeq \tilde{f}[n,m] &= \sum_{q=0}^{Q-1}\sum_{p=-P}^{P} F_p(p\Delta\Omega, q\Delta\theta)|p\Delta\Omega| \\ &\quad \cdot\exp[j\Delta\Omega p(n\Delta_x\cos(q\Delta\theta) + m\Delta_y\sin(q\Delta\theta))]. \end{aligned} \tag{6}$$

Equation (6) is a representation of the signal processing used in the CBP algorithm to compute $\tilde{f}[n,m]$ from $F_p(p\Delta\Omega, q\Delta\theta)$.

Now, a DF reconstruction scheme will be equivalent to CBP if the interpolation step in the DF scheme produces the 2-D DFT of $\tilde{f}[n,m]$ in Eq. (6). This follows, since the second step in the DF approach, an inverse 2-D DFT, would then produce $\tilde{f}[n,m]$. The 2-D DFT of $\tilde{f}[n,m]$ is

$$\begin{aligned} \tilde{F}[s,r] &= \sum_{n=-N}^{N}\sum_{m=-N}^{N} \tilde{f}[n,m]\exp\left[-j\left(\frac{2\pi}{2N+1}sn + \frac{2\pi}{2N+1}rm\right)\right] \\ &= \sum_{q=0}^{Q-1}\sum_{p=-P}^{P} F_p(p\Delta\Omega, q\Delta\theta)|p\Delta\Omega|\Delta\Omega\Delta\theta \\ &\quad \cdot\sum_{n=-N}^{N}\exp\left[-j\frac{2\pi n}{2N+1}\left(s - \frac{(2N+1)\Delta_x\Delta\Omega}{2\pi}p\cos(q\Delta\theta)\right)\right] \\ &\quad \cdot\sum_{m=-N}^{N}\exp\left[-j\frac{2\pi m}{2N+1}\left(r - \frac{(2N+1)\Delta_y\Delta\Omega}{2\pi}p\sin(q\Delta\theta)\right)\right]. \end{aligned} \tag{7}$$

Because the summation

$$\sum_{k=-N}^{N}\exp(-j\frac{2\pi}{L}k\omega) = \frac{\sin(\pi\omega)}{\sin(\pi\omega/L)}$$

[2]Generally, the truncated version of the filtering kernel $|p\Delta\Omega|$ is also replaced by a smoothed version [18]. We discuss this further in Section 4.

$$\stackrel{\text{def}}{=} \quad \text{asinc}(\omega, L), \tag{8}$$

where $L = 2N + 1$, is the periodic sinc, $\tilde{F}[s, r]$ can be expressed as

$$\begin{aligned}\tilde{F}[s,r] \;=\; & \sum_{q=0}^{Q-1} \sum_{p=-P}^{P} F_p(p\Delta\Omega, q\Delta\theta)|p\Delta\Omega|\Delta\Omega\Delta\theta \\ & \cdot\text{asinc}\left(s - \frac{(2N+1)\Delta_x \cdot \Delta\Omega}{2\pi} p\cos(q\Delta\theta), 2N+1\right) \\ & \cdot\text{asinc}\left(r - \frac{(2N+1)\Delta_y \cdot \Delta\Omega}{2\pi} p\sin(q\Delta\theta), 2N+1\right). \end{aligned} \tag{9}$$

The term $|p\Delta\Omega|\Delta\Omega\Delta\theta$ corresponds to the area of the cell of the sampling grid (see Figure 1), and so we note that the above equation corresponds to polar-to-Cartesian interpolation in the Fourier domain, using a 2-D periodic sinc-kernel with Jacobian weighting. Hence, the CBP algorithm is equivalent to the following two-step procedure:

- Step 1 : Polar-to-Cartesian interpolation in the Fourier domain using a 2-D periodic sinc-kernel interpolator with Jacobian weighting.
- Step 2 : Computation of the 2-D inverse DFT of the interpolated Fourier data.

In practice, we choose the parameters $\Delta_x, \Delta_y, \Delta\Omega$ and P to satisfy

$$\frac{(2N+1)\Delta_x\Delta\Omega}{2\pi}P < \frac{2N+1}{2} \quad \text{and} \quad \frac{(2N+1)\Delta_y\Delta\Omega}{2\pi}P < \frac{2N+1}{2}, \tag{10}$$

so that the periodic sincs in Eq. (9) are evaluated only on the central period where the periodic sinc is almost identical to a sinc. Thus, there is no significant difference between sinc and periodic-sinc interpolation in Eq. (9).

The CBP algorithm is one method of implementing the above two steps. A direct implementation of Step 1 requires $O(N^4)$ operations to reconstruct an $N \times N$ image from $N \times N$ Fourier data, if the interpolation kernel covers all available Fourier data. The CBP algorithm is a fast way of implementing the above two-step procedure in $O(N^3)$ operations. One minor difference between the CBP algorithm and the above two-step DF algorithm is that, in CBP, we usually use a 1-D interpolator to calculate the filtered projections at the precise locations needed to backproject to a rectangular grid. In the above two-step procedure, this interpolation is not necessary. In other words, the two-step procedure corresponds to using a perfect 1-D interpolator in the backprojection step of CBP.

3 Optimal Fourier-Domain Interpolator

In the previous section, we have shown that the CBP algorithm is equivalent to DF reconstruction, using a periodic sinc-kernel interpolator with Jacobian weighting. This form of interpolation is not optimal in any usual sense, which suggests that there may exist DF algorithms that can outperform the CBP method. For tractability, let us consider a squared error measure. In view of the discrete form of Parseval's relation, minimization of the total squared error in the spatial domain corresponds to minimization of the total squared error in the Fourier-domain. Hence, the least-squares optimal Fourier-domain interpolator would render the least-squares optimal reconstruction of the image.

The least-squares optimal interpolator was first proposed by Yen [16], and was later shown to be minimax optimal with respect to many other error norms [19, 20]. The extension of the Yen interpolator to two-dimensions is straightforward [21]. The use of the Yen interpolator for polar-to-Cartesian interpolation in the DF method would be expected to produce a better image than that produced by the CBP algorithm. However, to our knowledge, the Yen interpolator has never been tried in DF reconstruction for CT. This may be due to the heavy computational requirement of Yen interpolation. For example, processing a 512×512 image requires inversion of a 262144×262144 matrix. Numerical instabilities, and excessive computation time and memory requirements limit the utility of the full Yen interpolator and suggest the use of a block-Yen interpolator [22]. In the next section, we compare the CBP algorithm with the DF approach using full 2-D sinc interpolation, Hamming-weighted 2-D sinc interpolation, and block-Yen interpolation.

4 Simulations of Tomographic Reconstruction

We conducted a series of simulations to assess the reconstruction quality of various approaches to DF reconstruction in CT. In our simulations, we used the synthesized head phantom image whose gray-level distribution is given in [5]. Figure 2 shows the original 256×256 gray-scale image, which is to be reconstructed from its projection data. For proper reconstruction of a 256×256 image, it is known that the minimum number of necessary angular projections is $\frac{\pi}{2}256 \simeq 402$ [17, 23]. As the starting point for our simulations, we generated 402 projections of the head-phantom image with 512 samples for each projection. The sampled projections formed the input to the CBP algorithm. For the direct-Fourier reconstructions, we first computed the 1-D FFT of each projection to obtain Fourier transform samples on a uniform polar grid.

Figure 3 shows the image reconstructed using the CBP algorithm. A four-point interpolator was used to backproject the filtered projection data. The image quality is very good.

Figure 4 shows the result of using the DF method with the full 2-D periodic sinc-kernel interpolator with Jacobian weighting. This interpolator used all available polar Fourier data to estimate each Fourier sample on the Cartesian grid. In Section 2, this form of reconstruction was shown to be equivalent to CBP. We note that the reconstructed image is comparable to that produced by CBP. It is hard to distinguish this reconstruction from the original image in Fig. 2. However, reconstruction by this equivalent direct method required *far* more computation time to produce the same (approximately) image. This DF reconstruction required $O(N^4)$ operations while the CBP method is an $O(N^3)$ algorithm. This difference in complexity arises because, unlike the CBP algorithm, the DF method does not utilize the special structure of the sampling grid.

Because the full periodic sinc-kernel interpolator is computationally too expensive, a simplified version of the sinc-kernel interpolator is a better choice for DF reconstruction. Since the periodic sinc kernel decays rapidly within its period, we expect that data located far from the point to be interpolated will have little effect on the final result. Hence, it is reasonable to truncate the sinc kernel or to impose a finite-size data window. There are two ways of accomplishing this. One method is to base the interpolation on a fixed number of samples that are closest to the point to be interpolated. The other method is to consider a window of a fixed size and incorporate all samples falling inside the window. Through numerical simulation, we found that the second approach gives the better performance, so we consider only the second method here. In our simulations, the sinc-kernel was used instead of the periodic sinc-kernel. If the window size is small, this has virtually no effect on the final reconstructed image. To reduce the effect of abrupt truncation of the sinc kernel, we applied a Hamming window to the kernel. Hamming-windowing reduces the height of the sidelobes of the Fourier transform of the kernel, which in turn reduces the aliased component of the image due to imperfect filtering in the stopband of the truncated kernel. However, the effective frequency band of the kernel is broadened, and so the boundaries of the reconstructed image may experience more aliasing. Fortunately, the resulting deterioration of the image at the boundaries can often be ignored. In our simulations, we experimented with $n \times n$ windows with $n = 2, 4, 8$ and 16, where the window size was measured in terms of the spacing between zero-crossings in the sinc kernel. During the interpolation procedure, the number of Fourier data points falling within the window varied tremendously as a function of the window position. For positions near the center

of the polar grid, many more data samples fell within the window than for positions near the edge of the polar grid. Figure 5 shows the image reconstructed using a sinc kernel that was truncated by imposing a 4×4, 2-D Hamming window. Figure 6 is the resulting image using a 16×16 Hamming-windowed sinc kernel. We do not show the images for 2×2 and 8×8 windows, due to space limitation. The reconstructions become fairly hard to distinguish from the image in Fig. 4 as the size of the window increases. When the window size is small, the pixels near the boundaries of the image are noticeably shaded. To compensate for this, the brightness level of the final image can be adjusted correspondingly. This approach was used successfully in [8] and [9]. Table 1 lists the sum of squared errors for each reconstruction, with the original image in Fig. 2 serving as the baseline. We conclude that DF reconstruction, using a 2-D sinc-kernel interpolator of modest size, is only slightly inferior to CBP in terms of image quality. Using all available data, without windowing the sinc kernel, gives the smallest error. The CBP algorithm is an efficient means of accomplishing this. Our DF implementation using the 16×16 windowed sinc kernel did not save computation over the CBP approach.

In Footnote 2, we indicated that the truncated absolute value function in Eq. (6) is generally replaced by a smoother function in CBP implementations. To check the effect of this, we repeated the simulation for Fig. 3, except using the Shepp-Logan kernel [24]. The resulting reconstruction was very similar to Fig. 3, but with slightly reduced ringing and slightly blurred edges. The squared error was 22.08, virtually the same as for Fig. 3. We note that the truncated absolute value in Eq. (6) propagates through the algebra to Eq. (9). Thus, the Shepp-Logan (or other) kernel also can replace the absolute value in DF reconstruction. It is not necessary that DF reconstruction use Jacobian weighting. Notice that the weighting of the Fourier data in Eq. (9) occurs prior to the periodic sinc interpolation.

We next consider reconstructions using a block version of the Yen algorithm. When using block-Yen interpolators for DF reconstruction, we must regularize the algorithm to preserve numerical stability. The commonly used and simplest method of regularization is to add a small constant, ϵ, to the diagonal elements of the matrix appearing in the Yen algorithm, before inversion. The optimal value of ϵ is determined according to the SNR of the data [25]. In most practical cases, the SNR is not known exactly. For our simulations, we experimentally found a reasonable range of ϵ. Table 2 shows the squared error of the reconstructed image as a function of ϵ, for a 2 by 2 windowed block-Yen interpolator. We see that the choice of ϵ is not critical and that a value of

10^{-4} provides good results. The choice $\epsilon = 10^{-4}$ also worked well for larger window sizes up to 16×16. Thus, we chose $\epsilon = 10^{-4}$ for all our simulations using the block-Yen algorithm. Although regularization has the desired effect of increasing numerical stability, we note that it also has the effect of distorting the high-frequency components of the image [26], resulting in smoothing of edges in the reconstructed image.

We observed an important phenomenon when using the block-Yen algorithm. As the window size increased and the number of data samples incorporated in the interpolation increased, we expected to see smaller interpolation error. However, just the opposite often occurred. Once the number of data samples within the window increased beyond a certain point, we observed larger error. This increased error was apparently due to increased numerical instability as the size of the matrix inversion problem became larger [21, 27, 28]. This increasing instability of the Yen algorithm makes it impossible to achieve the expected performance, and severely limits the utility of Yen interpolation in practice. Hence, in an actual implementation of the block-Yen algorithm, we must somehow choose the size of the window properly, and at the same time, limit the number of samples incorporated in the interpolation. For our simulations, we obtained good results when the window size was 4×4, or less, and the maximum number of samples used for interpolation at each point was 300, or fewer. Many more than 300 samples could fall within the window for positions near the origin of the polar Fourier data. In such cases, we used the 300, or fewer, closest samples to the point being interpolated. Figures 7 to 10, and Table 3, give the results of our simulations. In Figures 7 and 8, a 2×2 block-Yen algorithm was applied, with a maximum of 50 and 300 samples used to compute each interpolated value, respectively. Figures 9 and 10 show the results using a 4×4 block-Yen algorithm. The images in Figs. 7-9 have obvious artifacts. Even the image in Fig. 10 is inferior to the image in Fig. 4. However, from Table 3, we see that the Yen algorithm produced squared errors that are much smaller than those for the other reconstruction methods. Thus, the block-Yen algorithm did perform very well in terms of squared error, as expected. Even with small window sizes, the block-Yen algorithms required a large amount of computation, because the size of the required matrix inversion became large for window positions near the center of the polar grid. When we increased the window size beyond 4×4, or the maximum number of samples beyond 300, the squared error increased, and the visual quality of the image didn't improve much from the image in Fig. 10. This is believed to be the result of increased numerical instability, as discussed earlier.

5 Direct-Fourier Reconstruction from a Concentric-Squares Grid

In Section 2, we showed that the CBP algorithm is equivalent to DF reconstruction using a Jacobian-weighted periodic sinc-kernel interpolator. The CBP algorithm reduces the amount of computation in CT image reconstruction by decomposing the 2-D problem into a succession of efficient 1-D operations (such as the FFT). It is notable that other tomographic reconstruction algorithms exist, which are even faster, and which provide reconstruction quality that is comparable or even superior to CBP. These faster algorithms require collection of Fourier data on a modified polar grid. In this section, we consider one such class of algorithms, which operates on a concentric-squares (CS) grid.

The usual polar grid in CT is obtained by collecting projections that are uniformly spaced in angle, and then computing an FFT of uniformly-spaced samples of each projection. However, by simple adjustment of the angles between different projections, and varying the sample spacing according to projection angle, we can obtain Fourier data on the CS grid as shown in Fig. 11. Notice that in Region II, for example, the projection angles θ_i are uniform in $\tan\theta_i$. Each point on the CS grid is a uniformly-spaced sample along two different straight lines (one radial, the other horizontal or vertical), which increases the possibility of using fast algorithms such as the FFT and chirp-z transform for tomographic inversion.

There have been several studies focused on the development of fast reconstruction algorithms for data lying on a CS grid. In [29], data on a uniform polar grid were interpolated to a modified CS grid, and then nearest-neighbor interpolation was applied to the perimeters of the modified CS grid to obtain Fourier data on a Cartesian grid. The shape of the grid was different from the one shown in Fig. 11 because the samples on the perimeters of the squares were distributed nonuniformly due to uniform angular spacing between projections. In [10, 11], the linogram reconstruction method was proposed, which uses a CS data grid, with the chirp-z transform applied along the perimeters of the squares to perform one step of the inverse 2-D Fourier transform. The CS concept has also been proposed in SAR [30, 31, 32, 33], where the grid becomes trapezoidal in shape. In SAR, inversion is accomplished using the chirp-z transform in the cross-radial direction and the FFT in the radial direction. Here, we evaluate the CS processing algorithm proposed in [34]. The linogram method in [10, 11] is very similar to the work in [34], but the linogram algorithm is less efficient in the Fourier inversion.

Suppose the image $f(x,y)$ to be reconstructed from projection data is spatially limited as before, with $f(x,y) = 0$ if $|x| > a$ or $|y| > b$. Let $F(X,Y)$ be the 2-D Fourier transform of $f(x,y)$. Then,

the Nyquist sample spacings in the Fourier domain, in X and Y, are

$$\begin{aligned} \Delta X &= \frac{2\pi}{2a} = \frac{\pi}{a} \\ \Delta Y &= \frac{2\pi}{2b} = \frac{\pi}{b}. \end{aligned} \tag{11}$$

To have Fourier samples with average sampling rates satisfying the Nyquist sampling conditions in X and Y, it is natural to choose the geometry of the CS grid so that perimeters of neighboring squares have spacings ΔX and ΔY in the X and Y variables, respectively, as shown in Fig. 11. We divide the Fourier data grid into Regions I - IV as shown. We require that the projection angles θ_i be equally spaced in $\tan\theta_i$ in Regions II and IV, and in $\cot\theta_i$ in Regions I and III. This angular spacing ensures that the radial traces in the Fourier domain will intersect the perimeters of squares on the CS raster at uniform intervals. To simplify the formulation, we assume that there are projection angles corresponding to the diagonal boundary lines between regions.

The details of the data grid, for Region I, are shown in Fig. 12. The Fourier-domain grid coordinates $(X, Y) = (u(i,k), v(i,k))$ are given by

$$\begin{aligned} u(i,k) &= A(k) + i \cdot B(k) \\ v(i,k) &= (k+1)\Delta Y \\ 0 \le i \le M/2 &\text{ and } 0 \le k \le R-1 \end{aligned} \tag{12}$$

with

$$\begin{aligned} A(k) &= -(k+1)\Delta X \\ B(k) &= \frac{2|A(k)|}{M/2} = \frac{4|A(k)|}{M} \end{aligned} \tag{13}$$

where M is the number of projections, and so $\frac{M}{2}+1$ is the number of radial traces within the region, and R is the number of concentric squares determined by the extent of the Fourier transform of $f(x,y)$ in the Fourier domain. We assume that the resulting Cartesian grid, after interpolation, has Nyquist spacing so that the Cartesian Fourier-domain grid from all four regions will be $(2R+1) \times (2R+1)$ in extent with sample spacings of ΔX and ΔY.

The Cartesian grid coordinates in Region I can be expressed as $(X, Y) = (U(i,k), V(i,k))$ with

$$\begin{aligned} V(i,k) &= (k+1)\Delta Y, \qquad 0 \le k \le R-1 \\ U(i,k) &= \Delta X \cdot i, \qquad -k-1 \le i \le k+1. \end{aligned} \tag{14}$$

Note that all of these positions lie on the perimeters of the squares of the original CS grid. The Fourier domain grids for Regions II - IV are developed analogously.

We assume that the interpolated Fourier samples lying in Region I are computed using only the samples on the CS grid that are in Region I, and similarly for other regions. This simplifies the computation enormously. This assumption is automatically satisfied when we use 2-D sinc kernel interpolation, because all the sample points in other regions coincide with zero crossings of the kernel when we interpolate to a point on a Cartesian grid in Region I. To make the algorithm practical, we collect a few more projections "outside" each region to improve the interpolation accuracy near the edges of each region. This is illustrated in Fig. 13 for Region I. The additional projection angles are chosen in a manner such that the angular spacing continues to be uniform in $\tan\theta$ or $\cot\theta$, depending on the region involved.

Now, for simplicity, we might consider applying a 1-D sinc-kernel interpolator to each row of data in Fig. 12 to produce data on a Cartesian grid in Region I. This series of 1-D interpolations can be performed in an extremely efficient manner, as explained below. Furthermore, for the data grid in Fig. 12, 1-D interpolation is equivalent to 2-D interpolation. To see this, consider interpolating the value at $(U(m,n), V(m,n))$, using Jacobian-weighted 2-D sinc-kernel interpolation:

$$\begin{aligned} F(U(m,n),V(m,n)) \quad \simeq \quad & \sum_{i=0}^{M/2}\sum_{k=0}^{R-1} W(i,k)F(u(i,k),v(i,k)) \\ & \cdot sinc(a(U(m,n)-u(i,k))sinc(b(V(m,n)-v(i,k))). \end{aligned} \tag{15}$$

where the weighting $W(i,k)$ represents the Jacobian (area) of the sampling grid and is given approximately as

$$W(i,k) \simeq B(k)\cdot\Delta Y. \tag{16}$$

Since we have $V(m,n)-v(i,k) = m\cdot\Delta Y = m\cdot\pi/b$ for some integer m, we have $sinc(b(V(m,n)-v(i,k)) = 0$ if $k \neq n$. Thus, we obtain

$$F(U(m,n),V(m,n)) \simeq \sum_{i=0}^{M/2} W(i,n)F(u(i,n),v(i,n))sinc(a(U(m,n)-u(i,n))). \tag{17}$$

Hence, the interpolation formula can be written as

$$F(U(m,n),V(m,n)) \simeq \Delta Y B(n)\sum_{i=0}^{M/2} F(u(i,n),v(i,n))sinc(a(U(m,n)-u(i,n))), \tag{18}$$

which corresponds to 1-D interpolation on each horizontal line of data of the CS grid in Region I. Since the interpolation in Eq. (18) is from a uniform grid (on the horizontal perimeter of a square) to another uniform grid (with different spacing), it can be computed efficiently using the chirp-z interpolation algorithm [35]. This algorithm actually uses a periodic-sinc kernel, but it,

nevertheless, provides an exceptionally accurate interpolation. By repeating chirp-z interpolation on all perimeters of the concentric squares, we obtain interpolated Fourier data on a Cartesian grid. A simple 2-D inverse FFT then reconstructs the image.

The fact that sample spacings along each radial line differ from line to line in Fig. 11 makes the collection of data on a CS grid difficult because it is impractical to adjust the spacings between sensors in a CT system. With additional processing, however, we can obtain Fourier data on a CS grid without much computational overhead. After collecting projections using uniform sensor spacings, and with the same angular spacings as on a CS grid, we can apply the chirp-z transform to each projection to obtain Fourier data on the CS grid.

To test the reconstruction quality provided by using chirp-z interpolation along the perimeters of the CS grid, we simulated such reconstructions for the head phantom image and compared the results with those of the CBP algorithm. Figure 14 shows the reconstruction using 512 projections. For each region of the Fourier domain on the CS grid, 10 extra projections were used to reduce the error near the edges as suggested in Fig. 13. We note from Fig. 14 that the image reconstructed from data on a CS grid, using chirp-z interpolation, is superb. Furthermore, the required amount of computation for the chirp-z approach is $O(N^2 \log N)$ for reconstruction of an $N \times N$ image, versus $O(N^3)$ or $O(N^4)$ for other algorithms with comparable reconstruction quality. Although we didn't show the image in this paper, a reconstruction using 256 projections was almost identical to the image using 512 projections and nearly indistinguishable from the original image. Table 4 shows the squared error values of the images reconstructed from CS grid data. We note that the errors are less than those obtainable using either CBP or the sinc-kernel interpolators, with a polar grid, as provided earlier in Table 1.

The CBP algorithm can also be applied to the projection data associated with a CS grid, by backprojecting the data on each radial line and adding the results together for all projections. In the backprojection step, the angular spacing between radial lines is a function of angle; this should be taken into account by appropriately weighting the data before backprojection. Another form of CBP algorithm results if we inverse Fourier transform the data on horizontal (or vertical) lines in Regions I and III (or II and IV) rather than on radial lines. The inverse transform of horizontal (vertical) lines of data can be performed by partitioning each Fourier region as shown in Fig. 15 for Region I. Each partition in Fig. 15 contains exactly one horizontal line of data. Partitioning of Regions II, III and IV can be considered similarly. The inverse transform is performed by weighting

each line of data with the sample spacing (Jacobian), followed by Fourier inversion, producing spatial-domain values on a Cartesian grid. In the inversion step, the offset of each partition ($k\Delta Y$ in Fig. 15) must be incorporated by multiplying by an appropriate exponential phase shift term, since the offset in the Fourier domain corresponds to exponential modulation with a linear-phase term in the spatial domain. This inversion of each slice of Fourier data can be performed using the chirp-z transform to obtain spatial-domain values with fixed sample spacing. After obtaining the 1-D inverse transform of a line of data, with horizontal spacing corresponding to the Cartesian grid in the spatial domain, the values on the Cartesian grid are computed by multiplying the data by the appropriate exponential terms. The results of all partitioned sections are added to produce the final reconstructed image. Calculation of the values on the Cartesian grid after the chirp-z transform, and the summation of the results from different partitions, can be accomplished efficiently using 1-D FFTs. It can be shown that this entire process is exactly equivalent to chirp-z interpolation along the perimeters of the original CS grid, followed by a 2-D inverse FFT. Furthermore, this reconstruction algorithm is simply the CT version of the SAR algorithm proposed in [30] and analyzed in [31, 32].

6 Reconstruction of SAR images

Spotlight-mode SAR collects data through a tomographic imaging mechanism that is similar to CT [13]. The data lie on a section of a polar[3] grid that is offset from the origin in the Fourier plane. Figure 16 shows the location of the Fourier data for a typical spotlight-mode SAR, where ω_0 is the center frequency of the radar signal, BW is the bandwidth, c is the speed of light, and θ is the range of angles through which the radar views the target. Since the SAR data lie on a polar grid, it is possible to use a modification of the CBP algorithm, for image reconstruction [13, 36].

In a conventional, non-foliage penetrating, spotlight-mode SAR, the center frequency of the radar signal is far larger than the bandwidth, so that the collected data lie within a thin annulus, far from the origin of the polar grid. Also, the data collection angle θ is very small – often a few degrees or less. These two facts imply that the polar data grid is almost Cartesian. Hence, we expect that a simple polar-to-Cartesian interpolation will suffice to provide excellent image quality, and that if θ is small enough, we may omit the interpolation step altogether. The true polar nature

[3] A uniform pulse-repetition frequency, with a straight-line flight path (instead of circular), would actually result in a nearly polar grid, where the radials are uniformly spaced in the tangent of the data collection angle.

of the sampling grid will cause some minor target shifting and smearing, but the error will be small when the data grid is nearly Cartesian. In the case of a trapezoidal grid, this error has been studied in [37].

Figures 17 through 20 show simulated SAR image reconstructions assuming center frequency $f_0 = 10$ GHz, frequency step $f_s = 4$ MHz and 256 frequency steps, giving a bandwidth-to-center frequency ratio of $BW/\omega_0 = 0.1024$. The data collection angle was chosen to be fairly large (for SAR), specifically $\theta \simeq 5.8672$ degrees, to best illustrate the positive effect of interpolation. Although, the location and shape of a typical SAR Fourier data region is illustrated in Fig. 16, for the simulations in this paper, we centered the Fourier data at the origin. Furthermore, we assumed real-valued reflectivity. This scenario provides a better test of the interpolators, since offset Fourier data of a complex valued reflectivity (the true radar model) will provide images that are speckled in appearance [14]. Figure 17 was generated by computing a 2-D inverse FFT of the Fourier data lying on a Cartesian grid. This is the image that would be obtained using perfect interpolation, so we use it as a benchmark for comparison of reconstruction quality. The polar data grid deviates substantially from a Cartesian grid. Thus, direct inversion of the data without interpolation produced a poor image, as shown in Fig. 18. To obtain a better reconstruction, the polar data can be interpolated onto a Cartesian grid prior to FFT inversion. Figure 19 shows the image obtained by interpolating the data onto a Cartesian grid, using a 4×4 Hamming-windowed sinc-kernel interpolation with Jacobian weighting. Figure 20 shows the image resulting from 4×4 block-Yen interpolation. The images in Figs. 19 and 20 are considerably better than the image in Fig. 18. Also, with a nearly Cartesian grid, there were no numerical instability problems with the Yen interpolator, and regularization was unnecessary. Furthermore, the 4×4 interpolators for SAR were much less computationally demanding than those for CT, since the Fourier grid in SAR has a nearly uniform density, resulting in many fewer data points, on average, within the interpolator window.

As the data collection angle decreases and the relative bandwidth of the radar signal becomes smaller, the Fourier data grid becomes closer to Cartesian. When we conducted simulations for a data collection angle and bandwidth that were 1/4 of those in the previous simulations ($\theta = 1.4668$ degrees, $BW/\omega_0 = 0.0256$), the reconstruction with no interpolation was almost indistinguishable from the original image. For this set of SAR parameter values, the data grid is nearly Cartesian, and all of the reconstructed images were very good. Table 5 shows the squared error for the

SAR images. The error values coincide with our observations made from the visual quality of the reconstructions.

In summary, low-order interpolators work well in DF reconstruction in SAR, because the SAR data grid is nearly Cartesian. We believe that this same fact explains the improved numerical stability of the Yen algorithm in SAR, versus CT.

7 Reconstruction from a Trapezoidal Grid in SAR

Spotlight-mode SAR imaging systems usually obtain Fourier data on a portion of a nearly polar grid. By simple adjustment of the timing in the A/D converters following the quadrature demodulator in the radar receiver, data can instead be obtained on a trapezoidal grid, which simplifies the processing. Such a grid is shown in Fig. 21. Typically, this data grid arises in an intermediate step of 2-D polar-to-Cartesian interpolation, if this interpolation is performed in a separable fashion. Applying 1-D interpolation along radial traces on a polar grid produces data on the trapezoidal grid, which can then be interpolated to a Cartesian grid by employing 1-D interpolation on the trapezoidal grid in the cross-radial direction. Properly adjusting the sample timing in the A/D converters obviates the need for radial interpolation. The cross-radial interpolation and inverse 2-D FFT can be performed extremely accurately and efficiently using the algorithm proposed by Lawton [30], and more completely characterized in [31, 32]. In [31], this algorithm was developed by manipulating a formula which approximates the samples of the inverse 2-D Fourier transform of the trapezoidal data. This formula is equivalent to DF reconstruction using a periodic sinc-kernel interpolator with Jacobian weighting.

The trapezoidal grid in SAR is a portion of the grid within a single CS region, such as shown in Fig. 12. Hence, CS interpolation and inversion techniques for CT can be used for trapezoidal grids in SAR. Specifically, 2-D periodic sinc-kernel interpolation can be implemented as a succession of 1-D chirp-z interpolations. The resulting algorithm can be shown to be exactly the same as the algorithm proposed in [30].

8 Conclusion

We have studied DF reconstruction methods in CT and SAR. In CT, DF methods are generally thought to provide inferior image quality to CBP. We showed, however, that CBP can be viewed as a

fast method of DF reconstruction, employing a periodic-sinc polar-to-Cartesian interpolator. Since sinc kernels are not optimal for interpolating from polar to Cartesian grids, this analysis suggested that DF methods may exist that are superior to CBP. We simulated a number of DF reconstruction methods, employing windowed-sinc kernels, and a block version of the optimal Yen interpolator. For window sizes of 16×16 for windowed-sinc kernels, and 4×4 for the block-Yen interpolator, we found that image quality was only slightly inferior to that provided by CBP. However, the computational effort was larger than that required by CBP. The block-Yen approach suffered from numerical instability. Regularized block-Yen interpolators provided images that had lower squared error than the CBP image, but which were judged inferior from a visual standpoint. The regularization resulted in smoothing of high-frequency components. We also considered fast algorithms for CT reconstruction from a CS grid. The resulting image reconstructions were superior to those produced by CBP, from a polar grid, in terms of both image quality and required computation.

In the case of SAR image formation, we showed that even simple interpolation algorithms produced excellent DF reconstructions. Comparing the CT and SAR reconstruction problems, the main difference lies in the shape of the Fourier sampling grid. The nearly Cartesian nature of the grid in SAR makes interpolation easier, so that DF inversion is attractive in SAR. Conversely, in CT, the complexity of the necessary interpolation is much higher, unless a CS approach is used. This explains the popularity of the CBP algorithm in CT. We believe, however, that the CS approach merits more serious consideration in practice.

All reconstruction algorithms discussed in this paper, except those using the Yen interpolator, can be considered as methods of implementing a two-step reconstruction procedure:

(i) Interpolation of non-Cartesian Fourier data, using a 2-D Jacobian-weighted sinc-kernel (or periodic sinc-kernel) interpolator,

(ii) 2-D inverse FFT.

In [27], the Jacobian-weighted sinc-kernel interpolator was shown to be a stable approximation to the optimal Yen interpolator. Hence, we conclude that the available tomographic reconstruction methods, including the CBP algorithm, are approximate, but stable methods of implementing the optimal DF reconstruction using the Yen interpolator. At least for CT, the Yen interpolator is impractical due to its numerical instability. Overall, the search for accurate and efficient tomographic reconstruction algorithms is equivalent to the search for accurate and efficient methods for approximating the optimal interpolator in DF reconstruction.

References

[1] R. M. Mersereau and A. V. Oppenheim, "Digital reconstruction of multidimensional signals from their projections," *Proceedings of the IEEE,* vol. 62, no. 10, pp. 1319-1338, October 1974.

[2] R. M. Mersereau, "Direct Fourier transform techniques in 3-D image reconstruction," *Comput. Biol. Med.,* vol. 6, pp 247-258, 1976.

[3] H. Stark, J. W. Woods, I. Paul and R. Hingorani, "Direct Fourier reconstruction in computer tomography," *IEEE Trans. on Acoustics, Speech, and Signal Processing,* vol. ASSP-29, no. 2, pp. 237-245, April 1981.

[4] H. Stark, J. W. Woods, I. Paul and R. Hingorani, "An investigation of computerized tomography by direct Fourier inversion and optimal interpolation," *IEEE Trans. on Biomedical Engineering,* vol. BME-28, no. 7, pp. 496-505, July 1981.

[5] S. X. Pan and A. C. Kak, "A computational study of reconstruction algorithms for diffraction tomography: interpolation versus filtered backprojection," *IEEE Trans. on Acoustics, Speech, and Signal Processing,* vol. ASSP-31, no. 5, pp. 1262-1275, October 1983.

[6] N. Niki, T. Mizutani, Y. Takahashi and T. Inouye, "A high-speed computerized tomography image reconstruction using direct two-dimensional Fourier transform method," *Systems, Computers, Controls,* vol. 14, no. 3, pp. 56-65, 1983.

[7] S. Matej and I. Bajla, "A high-speed reconstruction from projections using direct Fourier method with optimized parameters-an experimental analysis." *IEEE Trans. on Medical Imaging,* vol. MI-9, no. 4, pp. 421-429, December 1990.

[8] J. D. O'Sullivan, "A fast sinc function gridding algorithm for Fourier inversion in computer tomography," *IEEE Trans. on Medical Imaging,* vol. MI-4, no. 4, pp. 200-207, December, 1985.

[9] J. I. Jackson, C. H. Meyer, D. G. Nishimura, and A. Macovski, "Selection of a convolution function for Fourier inversion using gridding," *IEEE Trans. on Medical Imaging,* vol. MI-10, no. 3, pp. 473-478, September 1991.

[10] P. R. Edholm and G. T. Herman, "Linograms in image reconstruction from projections," *IEEE Trans. on Medical Imaging,* vol. MI-6, no. 4, pp. 301-307, December 1987.

[11] P. Edholm, G. T. Herman and D. A. Roberts, "Image reconstruction from linograms: Implementation and evaluation," *IEEE Trans. on Medical Imaging,* vol. MI-7, no. 3, pp. 239-246, September 1988.

[12] J. L. Walker, "Range-Doppler imaging of rotating objects," *IEEE Trans. on Aerospace and Electronic Systems,* vol. AES-16, no. 1, pp. 23-52, January, 1980.

[13] D. C. Munson, Jr., J. D. O'Brien and W. K. Jenkins, "A tomographic formulation of spotlight-mode synthetic aperture radar," *Proceedings of the IEEE,* vol. 71, no. 8, pp. 917-925, August, 1983.

[14] D. C. Munson, Jr. and J. L. C. Sanz, "Image reconstruction from frequency-offset Fourier data," *Proceedings of the IEEE,* vol. 72, no. 6, pp. 661-669, June 1984.

[15] C. V. Jakowatz, Jr., D. E. Wahl, P. H. Eichel, D. C. Ghiglia and P. A. Thompson, *Spotlight-Mode Synthetic Aperture Radar: A Signal Processing Approach.* Norwell, MA: Kluwer Academic Publishers, 1996.

[16] J. L. Yen, "On nonunifrom sampling of bandlimited signals," *IRE Trans. Circuit Theory,* vol. CT-3, pp. 251-257, Dec. 1956.

[17] M. Soumekh, "Band-limited reconstruction from unevenly spaced sampled data," *IEEE Trans. on Acoustics, Speech, and Signal Processing,* vol. ASSP-36, no. 1, pp. 110-122, Jan. 1988.

[18] A. Kak and M. Slaney, *Principles of Computerized Tomographic Imaging.* New York: IEEE Press, 1987.

[19] N. P. Willis and Y. Bresler, "Norm invariance of minimax interpolation," *IEEE Trans. on Information Theory,* vol. IT-38, no. 3, pp. 1177-1181, May 1992.

[20] R. G. Shenoy and T. W. Parks, "An optimal recovery approach to interpolation," *IEEE Trans. on Signal Processing,* vol. SP-40, no. 8, pp. 1987-1996, Aug. 1992.

[21] D. S. Chen and J. P. Allebach, "Analysis of error in reconstruction of two-dimensional signals from irregularly spaced samples," *IEEE Trans. on Acoustics, Speech, and Signal Processing,* vol. ASSP-35, no. 2, pp. 173-180, Feb. 1987.

[22] G. Calvagno and D. C. Munson, Jr., "A frequency-domain approach to interpolation from a nonuniform grid," *Signal Processing,* vol. 52, pp. 1-21, 1996.

[23] P. Rattey and A. Lindgren, "Sampling the 2-D Radon transform," *IEEE Trans. on Acoustics, Speech, and Signal Processing,* vol. ASSP-29, no. 5, pp. 994-1002, Oct. 1981.

[24] L. A. Shepp and B. F. Logan, "The Fourier reconstruction of a head section," *IEEE Trans. on Nuclear Science,* vol. NS-21, pp. 21-43, 1974.

[25] K. Miller, "Least squares methods for ill-posed problems with prescribed bound," *SIAM J. Math. Anal.,* vol. 1, pp. 52-74, Feb. 1970.

[26] E. J. Diethorn and D. C. Munson, Jr., "A linear, time-varying system framework for noniterative discrete-time band-limited signal extrapolation," *IEEE Trans. on Signal Processing,* vol. SP-39, no. 1, pp. 55-68, Jan. 1991.

[27] H. Choi and D. C. Munson, Jr., "Analysis and design of minimax-optimal interpolators," *Proceedings of IEEE International Conference on Acoustics, Speech, and Signal Processing,* Detroit , MI., pp. 885-888, May 8-12, 1995.

[28] H. Choi and D. C. Munson, Jr., "Analysis and design of mimimax-optimal interpolators," submitted for publication to *IEEE Trans. on Signal Processing.*

[29] F. Natterer, *The Mathematics of Computerized Tomography.* Stuttgart: Wiley, 1986.

[30] W. Lawton, "A new polar Fourier transform for computer-aided tomography and spotlight synthetic aperture radar," *IEEE Trans. on Acoustics, Speech, and Signal Processing,* vol. ASSP-36, no. 6, pp. 931-933, June 1988.

[31] O. Arikan and D. C. Munson, Jr., "Analysis and simulation of a new algorithm for spotlight-mode synthetic aperture radar," *Proceedings of IEEE International Conference on Acoustics, Speech and Signal Processing,* Glasgow, Scotland, vol. 3, pp. 1453-1455, 1989.

[32] O. Arikan and D. C. Munson, Jr., "Further results on a new $O(N^2 \log N)$ algorithm for spotlight-mode SAR," *Proc. 1989 SPIE Conference on Millimeter Wave and Synthetic Aperture Radar,* Orlando, FL, pp. 23-33, March 27-28, 1989.

[33] J. W. Adams, R. W. Bayma, M. E. Lawrence, and L. Petrosian, "On the modified chirp z transform for synthetic aperture radar systems," *IEEE Trans. on Signal Processing,* vol. SP-39, no. 4, pp. 953-955, April 1991.

[34] K. J. Moraski and D. C. Munson, Jr., "Fast tomographic reconstruction using chirp-z interpolation," *Proceedings of 25th Asilomar Conference on Signals, Systems, and Computers,* Pacific Grove, CA, pp. 1052-1056, Nov. 1991.

[35] O. Arikan and D. C. Munson, Jr., "Interpolation between two uniform grids", *Proceedings of 1990 Bilkent International Conference on New Trends in Communication, Control and Signal Processing,* Ankara, Turkey, pp. 1044-1058, July 2-5, 1990.

[36] M. D. Desai and W. K. Jenkins, "Convolution backprojection image reconstruction for spotlight mode synthetic aperture radar," *IEEE Trans. on Image Processing,* vol. IP-1, no. 4, pp. 505-517, October, 1992.

[37] O. Arikan and D. C. Munson, Jr., "An analysis of keystone format spotlight mode synthetic aperture radar," *Proceedings of 21st Asilomar Conference on Signals, Systems, and Computers,* Pacific Grove, CA, pp. 690-694, Nov. 2-4, 1987.

[38] R. Mersereau, "Recovering multidimensional signals from their projections," *Comput. Graphics Image Processing,* vol. 1, pp. 179-195, October, 1974.

Reconstruction Method	Squared Error
Convolution Backprojection	21.79
Full periodic Sinc interpolation	21.77
2×2 Sinc interpolation	39.19
4×4 Sinc interpolation	35.34
8×8 Sinc interpolation	23.01
16×16 Sinc interpolation	21.96

Table 1: Squared error of reconstructed images - CBP, and DF with sinc interpolation

ϵ	Squared Error
10^{-6}	30750
10^{-5}	322.7
10^{-4}	12.32
10^{-3}	13.54
10^{-2}	21.74

Table 2: Squared error of reconstructed images - block-Yen algorithm

Window Size	Max. No. of Samples	Squared Error
2 by 2	50	12.32
	300	10.65
4 by 4	50	12.85
	300	10.90

Table 3: Squared error of reconstructed images - block-Yen with $\epsilon = 10^{-4}$

No. of Projections	Squared Error
512	16.24
256	16.76

Table 4: Squared error of reconstructed images - CS grid

θ	Interpolator	Squared Error
5.8672°	None	7.98
	4 by 4 Sinc	2.31
	4 by 4 block-Yen	1.91
1.4668°	None	0.27
	4 by 4 Sinc	0.25
	4 by 4 block-Yen	0.29

Table 5: Squared error of reconstructed images - SAR

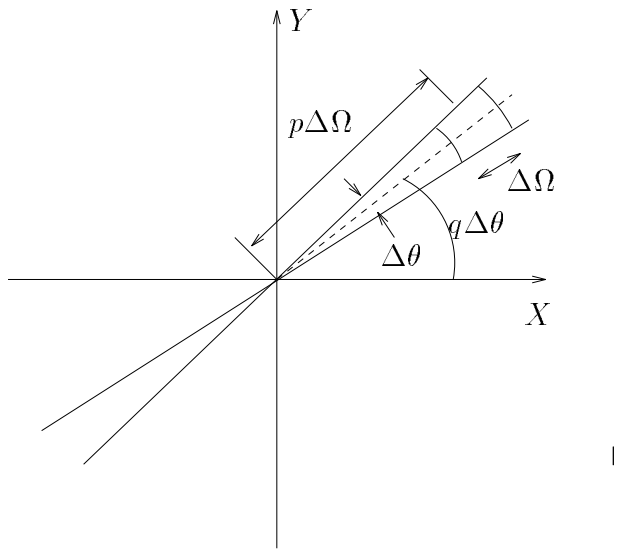

Figure 1: Fourier grid cell

Figure 2: Original image.

Figure 3: CT reconstruction produced by CBP algorithm.

Figure 4: CT reconstruction produced by equivalent direct-Fourier method.

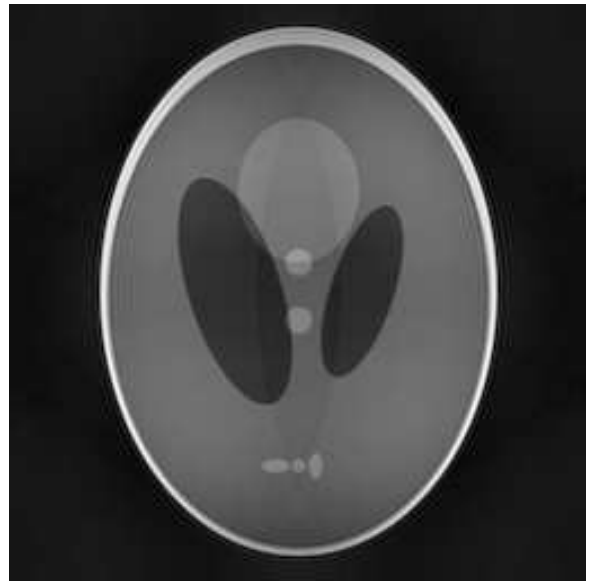

Figure 5: CT reconstruction produced by direct-Fourier method using 4×4 sinc interpolator.

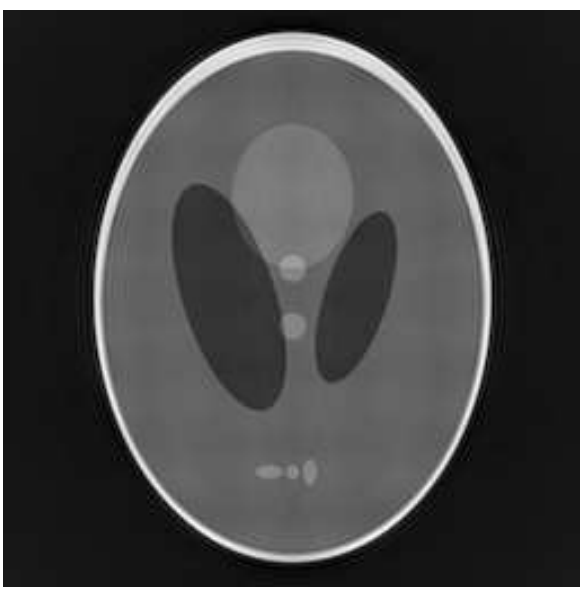

Figure 6: CT reconstruction produced by direct-Fourier method using 16×16 sinc interpolator.

Figure 7: CT reconstruction produced by direct-Fourier method using 2×2 Yen interpolator, 50 samples maximum, $\epsilon = 10^{-4}$.

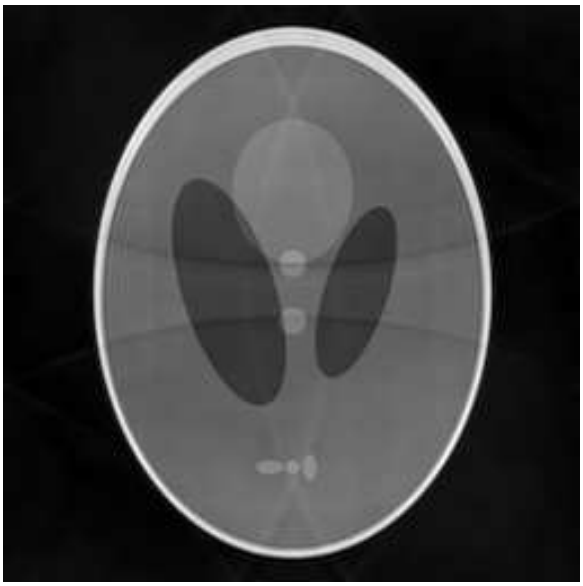

Figure 8: CT reconstruction produced by direct-Fourier method using 2×2 Yen interpolator, 300 samples maximum, $\epsilon = 10^{-4}$.

Figure 9: CT reconstruction produced by direct-Fourier method using 4×4 Yen interpolator, 50 samples maximum, $\epsilon = 10^{-4}$.

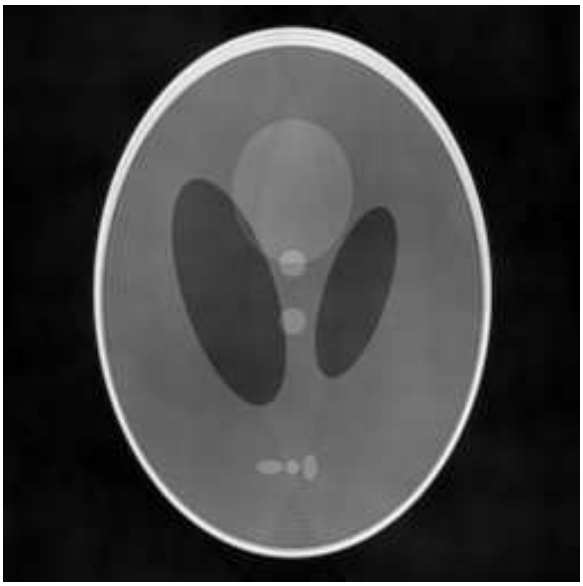

Figure 10: CT reconstruction produced by direct-Fourier method using 4×4 Yen interpolator, 300 samples maximum, $\epsilon = 10^{-4}$.

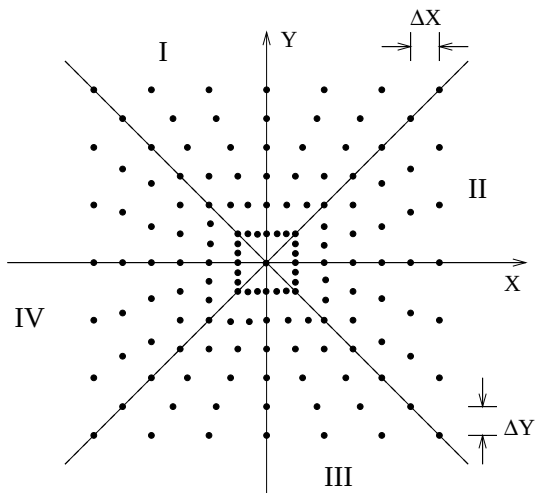

Figure 11: Concentric-squares grid

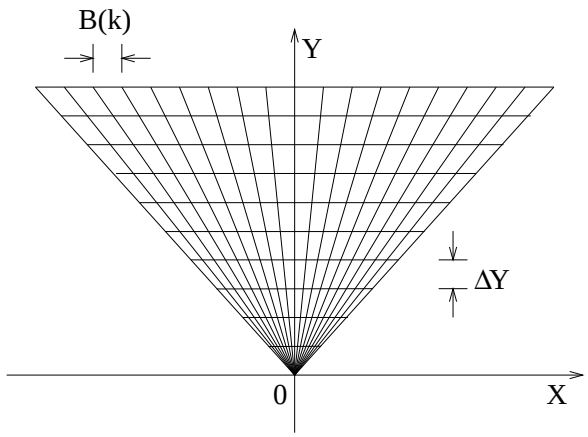

Figure 12: Region I grid

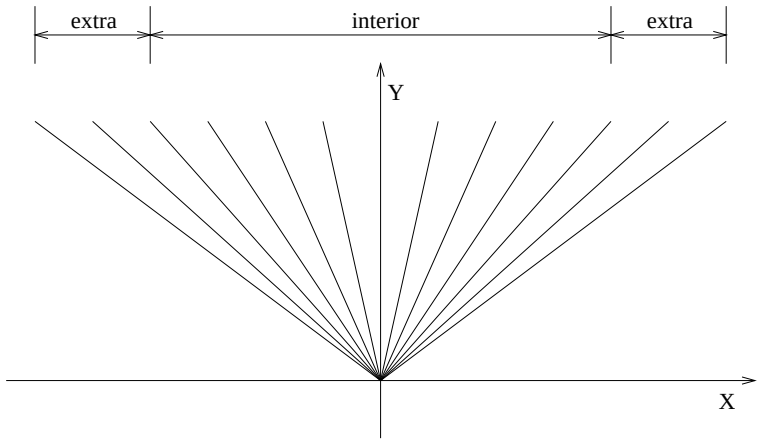

Figure 13: Extra projections in Region I

Figure 14: CT reconstruction produced by chirp-z algorithm from CS grid with 512 projections.

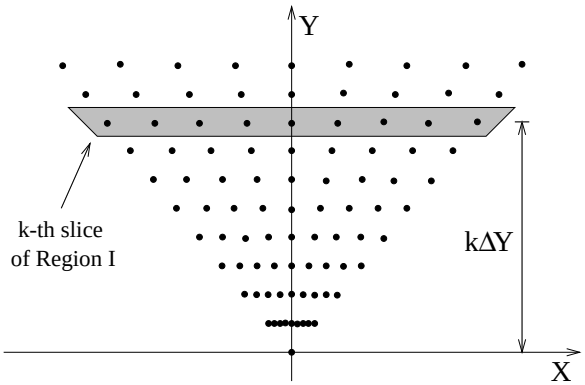

Figure 15: Partitioning of Region I

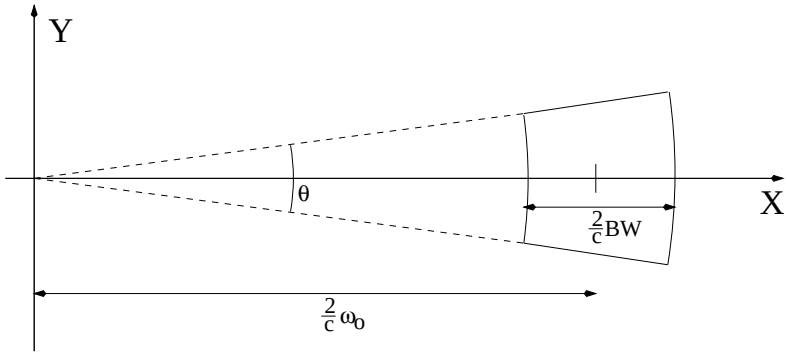

Figure 16: Location of SAR data on the Fourier plane

Figure 17: SAR reconstruction from Cartesian Fourier data, $BW/\omega_0 = 0.1024$, $\theta = 5.8672$ degrees.

Figure 18: SAR reconstruction from polar data, without interpolation, $BW/\omega_0 = 0.1024$, $\theta = 5.8672$ degrees.

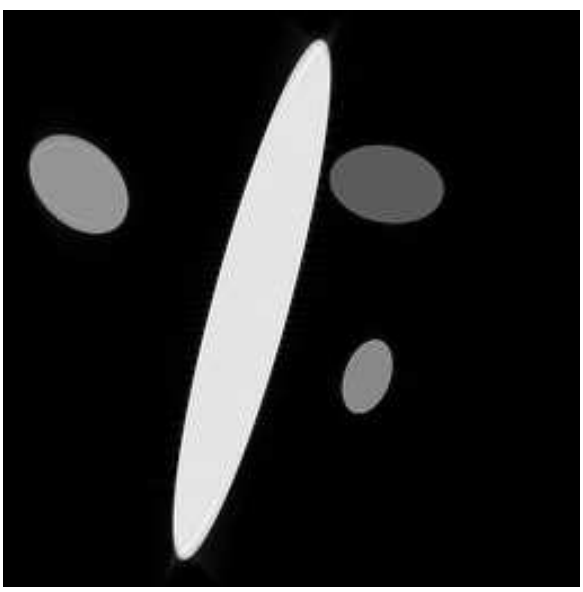

Figure 19: SAR reconstruction with 4×4 sinc interpolator, $BW/\omega_0 = 0.1024$, $\theta = 5.8672$ degrees.

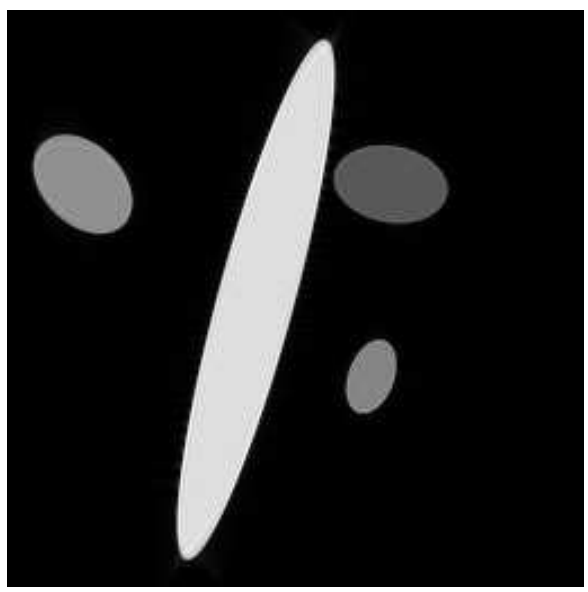

Figure 20: SAR reconstruction with 4×4 Yen interpolator, $BW/\omega_0 = 0.1024$, $\theta = 5.8672$ degrees.

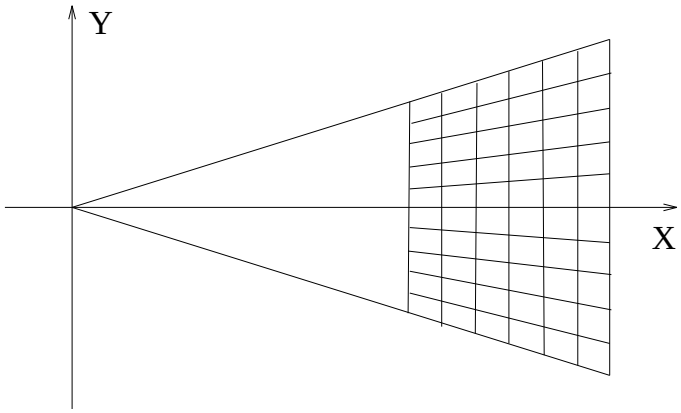

Figure 21: Trapezoidal grid in Fourier domain